Geotechnical
Testing Journal

Graeme Beardsmore,[1] Shannon Egan,[2] and Mike Sandiford[3]

DOI: 10.1520/GTJ20180300

A Fourier Spectral Method to Measure the Thermal Diffusivity of Soil

Geotechnical Testing Journal

doi:10.1520/GTJ20180300 available online at www.astm.org

Graeme Beardsmore,[1] Shannon Egan,[2] and Mike Sandiford[3]

A Fourier Spectral Method to Measure the Thermal Diffusivity of Soil

Reference

G. Beardsmore, S. Egan, and M. Sandiford, "A Fourier Spectral Method to Measure the Thermal Diffusivity of Soil," *Geotechnical Testing Journal* https://doi.org/10.1520/GTJ20180300

Manuscript received September 20, 2018; accepted for publication May 10, 2019; published online July 10, 2019.

[1] School of Earth Sciences, University of Melbourne, L4 McCoy Building, Parkville, Victoria, 3010, Australia (Corresponding author), e-mail: g.beardsmore@unimelb.edu.au, https://orcid.org/0000-0003-4812-1146

[2] Hot Dry Rocks Pty Ltd, L1 253–283 Elgin St., Carlton, Victoria, 3053, Australia

[3] School of Earth Sciences, University of Melbourne, L4 McCoy Building, Parkville, Victoria, 3010, Australia, https://orcid.org/0000-0002-9757-745X

ABSTRACT

It is well established that amplitude decays and phase shifts as a function of depth, frequency, and thermal diffusivity when a periodic surface temperature signal conducts into the ground. In historical practice, this principle has often been employed to estimate soil thermal diffusivity using observations of the dominant diurnal and annual temperature signals. We describe and demonstrate a method to infer thermal diffusivity over a broad bandwidth in the frequency domain using high fidelity time-series ground temperature records. We draw information from thermal signals generated by meteorological events over weeks and months, as well as the dominant diurnal signal. Both the decay in amplitude and shift in phase of each frequency band contribute points to plots that define linear functions relative to a parameter that incorporates frequency and depth. Linear regression through the points gives the magnitude and uncertainty of the slope of the function, where the slope is equal to the inverse square root of the average thermal diffusivity over the sampled time-period and depth interval. This allows statistical quantification of the uncertainty in the thermal diffusivity estimate. Furthermore, our method delineates depth intervals where nonconductive processes significantly affect heat transfer. Examples are presented for a dry desert soil in South Australia and the floor of a tropical alpine forest in Mexico.

Keywords

soil thermal diffusivity, Fourier analysis, ground temperature records

Introduction

Thermal diffusivity is the physical property that controls the rate at which the temperature of a medium changes in response to an applied heat source (or sink). It is often denoted by the Greek κ and is expressed in units of area per unit of time: square meters per second

(m^2/s). ASTM E1461, *Standard Test Method for Thermal Diffusivity by the Flash Method* (ASTM International 2013), and ASTM E1952, *Standard Test Method for Thermal Conductivity and Thermal Diffusivity by Modulated Temperature Differential Scanning Calorimetry* (ASTM International 2017), describe standard test methods for measuring the thermal diffusivity of homogeneous, nonporous, isotropic solid materials under laboratory conditions. Soil rarely, if ever, meets these conditions. Thermal diffusivity of competent rock and soil specimens can be directly measured under laboratory conditions using optical scanning techniques (e.g., Popov et al. 2016), probes that introduce and monitor transient heat pulses (e.g., Singh and Rao 1998), observations of heat pulses through slabs (e.g., Middleton 1993), or other techniques. Alternatively, ASTM D4612, *Standard Test Method for Calculating Thermal Diffusivity of Rock and Soil*, and (for example) Bording, Nielsen, and Balling (2016) describe methods to calculate thermal diffusivity from independent measurements of thermal conductivity (k, W/(m K)) and volumetric heat capacity ($\rho \cdot c_p$, J/(m^3 K)), where:

$$\kappa = \frac{k}{(\rho \cdot c_p)} \tag{1}$$

Laboratory-based measurements of recovered core specimens are often the only practical way to characterize the thermal diffusivity of very thick or deep intervals of rock, but specimens of soil or rock exhumed and transported to a laboratory provide, at best, an estimate of thermal diffusivity at a specific time and point in space. Such specimens may not represent the full interval of interest, and their temperature, porosity, and fluid saturation might change from in situ conditions during exhumation, transport, and preparation. This is particularly the case when an interval of interest is strongly heterogeneous, poorly consolidated, prone to temporal variation, or a combination of these factors. The near-surface layers of the Earth often fall into these categories, so in situ measurements of thermal diffusivity of the shallow subsurface are preferable.

Koo and Song (2008) and Rajeeva and Kodikara (2015) summarized the value and challenges of determining the in situ thermal diffusivity of the top several meters of soil. They described applications for such measurements in agricultural engineering, designing ground heat exchange systems, and understanding energy fluxes for climate modeling. Singh and Rao (1998) noted other applications related to laying underground power cables and oil/gas pipelines. While rarely, if ever, explicitly discussed, we infer that half an order of magnitude is probably acceptable precision for diffusivity estimates for these applications. Saavedra and Takahashi (2017) showed soil thermal diffusivity to be an important variable for predicting the course of frost events, and Cheng et al. (2014) illustrated its importance for modeling freeze-thaw cycles. More precise estimates of diffusivity on the order of ±25 % might be required for meaningful predictions for these applications. Our own work was motivated by a need to predict the diffusion of time-varying surface temperature to a depth of 1.10 m with a precision and accuracy on the order of millikelvin, for which we need diffusivity estimates with uncertainties less than ± 5 %. We will report on those experiments in a future article. This article presents a methodology for an explicit determination of in situ thermal diffusivity and uncertainty for the shallow subsurface.

Rajeeva and Kodikara (2015) summarized five previously published methods for estimating in situ thermal diffusivity of soil based on analytical solutions of the one-dimensional heat flow equation. They obtained their most accurate results (relative to values obtained from laboratory measurements of thermal conductivity and volumetric heat capacity, coupled with in-field soil moisture records) from a "harmonic equation" method that jointly assessed the behavior of the first three harmonic components of the Fourier series of concurrent time-temperature records from different depths to 2 m. They primarily interpreted the annual temperature cycle sampled at 10-minute intervals over one full year. They did not quote uncertainties for their results but rather validated their inferred values of thermal diffusivity by predicting the diffusion of the subsequent year of recorded surface temperatures, comparing their predictions against observed subsurface temperatures. They found absolute average differences less than 1°C between measured and predicted temperatures, which, for them, represented "very good agreement over the measured period at all the depths." However, ±1°C precision is two to three orders of magnitude too coarse for our own application in which we aim to detect and quantify the geothermal gradient upon which the diffused surface signal is superimposed. Given that the geothermal gradient should typically be less than 0.1°C/m in the top meter of soil, we require an absolute accuracy on the order of ±0.01°C in our temperature predictions and even greater precision.

Two of the methods assessed by Rajeeva and Kodikara (2015) related to quantifying and interpreting the decay in amplitude and shift in phase, respectively, of a regular sinusoidal temperature signal applied to the surface of a purely conductive half-space. They concluded that these two techniques often yielded different estimates of thermal diffusivity, especially at shallow depths. Koo and Song (2008) applied the same two methods to interpret thermal diffusivity to a depth of 5 m using temperature data recorded daily in a series of boreholes in South Korea over a 21-year period from 1981 to 2002. They also found that the phase and amplitude methods gave significantly different results shallower than 0.5 m but were relatively consistent at greater depths. Koo and Song (2008) did not explicitly report the precision or accuracy of their derived thermal diffusivity values.

Specifications of our application that distinguish it from previous studies include:

- Our temperature records extend for months, rather than years,
- We aim for ±1 % precision and accuracy in thermal diffusivity,
- We only monitor the top 1.10 m of the ground.

The conclusions of prior studies, i.e., that phase and amplitude of cyclic temperature signals behave in a manner inconsistent with a single value of thermal diffusivity at shallow depths, were important for our work. However, given that we do not adequately sample the dominant annual temperature signal in our application, we required a new methodology based on sampling periods of weeks to months.

Theoretical Basis of Method

When a sinusoidal periodic temperature cycle is applied to the surface of a purely conductive half-space, the amplitude and phase of the induced temperature signal at depth, z, within the medium can be shown to be related according to:

$$\ln\left(\frac{A_0}{A_z}\right) = \Delta\phi = \frac{1}{\sqrt{\kappa}} \cdot \sqrt{z^2 \cdot \pi \cdot f} \tag{2}$$

where:

z = depth, m,

A_0 = amplitude of the surface temperature cycle, K,

A_z = amplitude of the temperature cycle induced at depth z, K,

$\Delta\phi$ = phase lag of the induced cycle relative to the surface cycle, radians,

f = frequency of the surface cycle, Hz, and

κ = thermal diffusivity of the medium, m^2/s.

In principle, the $z = 0$ "surface" can lie at any arbitrary depth, so equation (2) provides a theoretical basis from which to infer the average thermal diffusivity between any two temperature sensors recording over the same time period and frequency range.

Equation (2) describes two linear functions. The first is between the natural log of the inverse of amplitude decay and $\sqrt{z^2 \cdot \pi \cdot f}$, and the second is between phase shift and $\sqrt{z^2 \cdot \pi \cdot f}$. For a purely conductive medium, the two relationships have the same slope, are equal to $1/\sqrt{\kappa}$, and pass through the origin. Amplitude or phase information for a single frequency is sufficient to estimate κ, but a single frequency provides no information about uncertainty. Simultaneously evaluating amplitude or phase data for more than one frequency allows statistical quantification of the mean and standard error of the calculated diffusivity. Increasing the number of individual frequencies evaluated would normally narrow the uncertainty range and increase confidence in the result.

A temperature signal sampled at regular intervals over a finite period can be decomposed into discrete frequency components using a discrete Fourier transform. A discrete Fourier transform converts a sample of N temperatures recorded at a constant rate of f_s Hz into N frequency bins at steps of Δf Hz where:

$$\Delta f = f_s / N \tag{3}$$

The bins cover a frequency range from $-(N/2)\cdot\Delta f$ – $(N/2-1)\cdot\Delta f$ if N is even, or $-((N-1)/2)\cdot\Delta f$ – $((N-1)/2)\cdot\Delta f$ if N is odd. For example, a data set of temperatures sampled at regular 6-hour intervals ($f_s = 4.6296 \times 10^{-5}$ Hz) for exactly 100 d would contain $N = 401$ samples (the first sample at time-zero). A discrete Fourier transform of this data set would produce 401 frequency bins at steps of $\Delta f = 1.1545 \times 10^{-7}$ Hz and would span a spectrum from -2.3090×10^{-5} Hz – 2.3090×10^{-5} Hz.

Recorded temperatures are always "real" values, so only $N/2$ frequency bins, if N is even, or $(N+1)/2$ bins, if N is odd, hold useful information. These bins correspond to a constant value at zero frequency, plus all the positive frequencies that define the variation of the signal from that constant value over time. Negative frequency bins are complex conjugates of the positive frequencies. They hold redundant information and can be ignored. Each positive bin is characterized by a complex number, $a + ib$, the magnitude ($\sqrt{(a^2+b^2)}$) of which is "amplitude" in kelvin, the angle ($\tan^{-1}(\frac{b}{a})$) of which is "phase" in radians. Frequency, amplitude, and phase together define a harmonic cosine wave. When normalized by a factor of $2/N$ (where N is the number of samples in the original time series), the amplitudes represent the true magnitude of each frequency's contribution to the original signal. All waves with amplitudes greater than "background noise" are potentially useful for estimating thermal diffusivity.

Diurnal and annual cycles dominate the near-surface temperature signal in most locations. However, chaotic weather patterns introduce a wide range of other harmonic frequencies to the surface temperature signal. We show that several months of temperature records contain significant information across many frequencies from which estimates of in situ soil thermal diffusivity can be derived with quantified uncertainty.

Equipment and Processing Methodology

EQUIPMENT

Beardsmore (2012), Beardsmore and Antriasian (2015), and Beardsmore et al. (2017) described the design and calibration of the instruments we used to record ground temperature. Deployment involved inserting a 16-mm-diameter hollow stainless steel casing vertically into the ground (**fig. 1*A***), filling the casing with mineral oil, and inserting a string of temperature sensors into the casing. Each sensor contained a thermistor positioned to 0.001 of 0.00 m, 0.10, 0.30, 0.50, 0.70, 0.90, or 1.10 m subsurface. Each thermistor was integrated onto an independent electronic circuit board measuring 9.5 × 58.5 mm (**fig. 1*B***) and containing a Wheatstone bridge circuit, digital controller, and analog-digital converter. The temperature signal was fully digitized in situ and only power and digital signals were passed in series along the sensor string to and from an externally mounted battery, controller, and memory unit (**fig. 1*C***). In this way, random signal noise inherent in measuring resistance across thermistors through copper wires was avoided, yielding high-fidelity temperature measurements. The digital response of each circuit board to temperature was empirically calibrated against a precision digital thermometer in a temperature-controlled oil bath following the procedure described by Beardsmore and Antriasian (2015), to provide ±0.0003 K precision and ±0.003 K absolute accuracy on temperature measurements over the range 0°C–50°C.

PROCESSING METHODOLOGY

Our data sets consisted of temperatures measured simultaneously at precise depths (0.00, 0.10, 0.30, 0.50, 0.70, 0.90, and 1.10 m) at a single location every 900 s (15 minutes). Our processing approach was to apply discrete Fourier transforms to the records, to identify frequencies with significant amplitudes, to apply equation (2) to the phases and amplitudes of those frequencies, and to chart the relationships versus $\sqrt{z^2 \cdot \pi \cdot f}$.

FIG. 1 (*A*) Drilling 16-mm-diameter hollow casing into the ground, (*B*) digital temperature sensor circuit measuring 58.5 × 9.5 mm, (*C*) inserting string of sensors and logger unit into casing.

(*A*) (*B*) (*C*)

Fourier transform methods interpret finite time-series data as infinite repetitions of the record. Significant offsets in signal magnitude or trend between the start and end of a temperature record can introduce spectral artifacts in the frequency domain. We trialed several standard approaches to minimize this effect on our signals and found that applying a Hanning window (as described by Harris 1978) to our temperature records prior to the Fourier transform offered the best results for minimizing spectral noise.

A Hanning window produces a modified temperature signal by tapering the beginning and end of the temperature record to zero magnitude with a smooth cosine function:

$$T_H(n) = T(n) \cdot \frac{1}{2}\left(1 - \cos\left(\frac{2\pi n}{N-1}\right)\right) \tag{4}$$

where:

$T_H(n)$ = modified temperature of the nth sample,

$T(n)$ = initial temperature of the nth sample, and

N = total number of samples in the record.

While minimizing spectral noise, a Hanning window overprints the lower frequency features of the original signal. We found that this had minimal impact on our results as most information lay in the midfrequency bands of our signals.

After applying a Hanning window to each temperature series, we transformed the modified records into the frequency domain using the Python module for Fast Fourier Transforms (FFT), numpy.fft. Our records at each depth were collected using the same sampling interval over the same period, so the resulting amplitude and phase spectra comprised the same set of frequency bins for each depth. We retained only the positive frequency parts of the complex conjugates for further processing. From these, we identified and retained frequencies with amplitudes exceeding a subjectively determined minimum amplitude, as described in greater detail in the Results section below. For different pairs of sensors, we calculated the natural log of the amplitude ratio and the apparent phase shifts of each retained frequency.

The final processing steps involved charting amplitude decay and phase shift against $\sqrt{z^2 \cdot \pi \cdot f}$ and fitting a line of best fit through each set of points using the Python module for least squares linear regression, numpy.linalg.lstsq. The inverse square of the slope of each line yielded the apparent thermal diffusivity value for the associated parameter (amplitude or phase) and depth interval as defined by equation (2), whereas the uncertainty in the slope provided information on the uncertainty in the diffusivity value.

Data

We tested the methodology for two sites selected from the limited data sets available to us. We selected the two sites to confirm that the methodology would work across very different climates, regolith types, and record lengths. Knowledge of the soil type and layer thicknesses are not required to calculate thermal diffusivity profiles using our methodology, although such knowledge would aid in attributing physical causes to the results.

The first set of data ("Carrapateena"; 31.21808°S, 137.49747°E; Beardsmore 2018a) was from desert terrain covered by low and sparse salt bush and rock fragments up to cobble size near the Carrapateena mine development camp in South Australia (fig. 2). The climate was semiarid with summer daytime maximum temperatures exceeding 45°C, winter nighttime minimum temperatures less than 10°C, and low rainfall. Craig (2013) characterized the topsoil at the site as "terrestrial regolith including undifferentiated sediments of mixed colluvial, alluvial, aeolian, lacustrine or unknown origin, some Cenozoic and palaeo-channel sediments." The site was not augured and no other information was available about the exact type or thickness of soil layers, although traces of red clay and silcrete returned to the surface as we drilled our instrument into the soil.

Temperature was recorded at six depths between 0.10 and 1.10 m over eight and a half months from December 2012 – August 2013 (fig. 3). The data set consisted of $N = 24{,}931$ measurements for each depth. The 0.10 m sensor recorded daily peak–trough temperature amplitudes of about 10 K, and a summer–winter difference in mean temperature close to 20 K.

The second set of data ("Puebla"; 19.92216°N, 98.12475°W; Beardsmore 2018b) was obtained from a pine forest on the outskirts of the township of Cruz Colorada, Puebla, Mexico, over a 5-month period from March – September 2015. The site was on a steep slope almost entirely shaded by the pine trees (fig. 4). The site was not augured and no other information was available about the exact type or thickness of soil layers, although

FIG. 2

The site in South Australia at which the Carrapateena data set was collected.

FIG. 3 The Carrapateena temperature record. Data from Beardsmore (2018a).

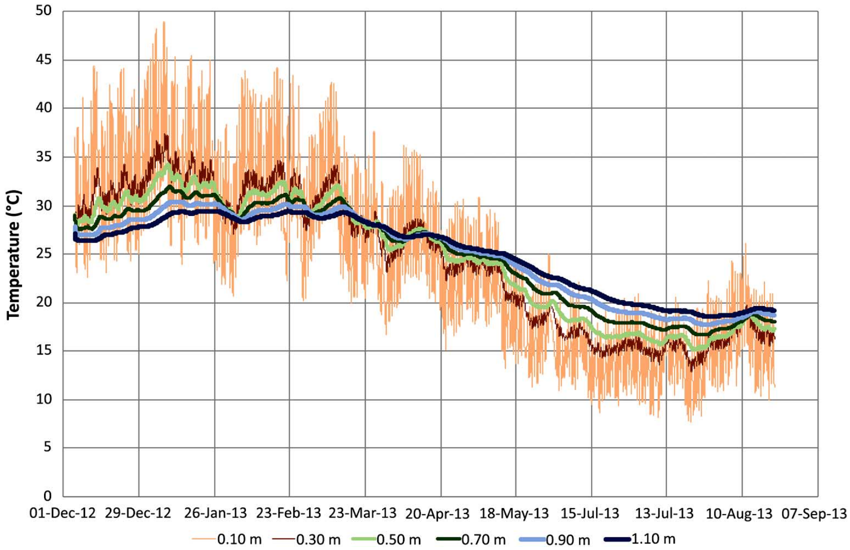

FIG. 4 The site in Mexico at which the Puebla data set was collected.

fragments of pine needle humus then rocky soil returned to the surface as we drilled our instrument into the soil. Seven temperature records were collected from 0.00 – 1.10 m subsurface (fig. 5).

The data set consisted of $N = 16{,}314$ measurements for each depth. The 0.00-m sensor recorded a daily temperature cycle with an amplitude of 5–10 K and showed little evidence of any significant annual temperature cycle.

Results

From the Fourier spectra of the signals for each site, we identified frequencies with amplitudes greater than background noise. For those frequencies, we investigated the amplitude, $\ln(\frac{A_0}{A_z})$, and phase, $\Delta\phi$, trends with respect to $\sqrt{z^2 \cdot \pi \cdot f}$, for pairs of signals.

FIG. 5 The Puebla temperature record. Data from Beardsmore (2018b).

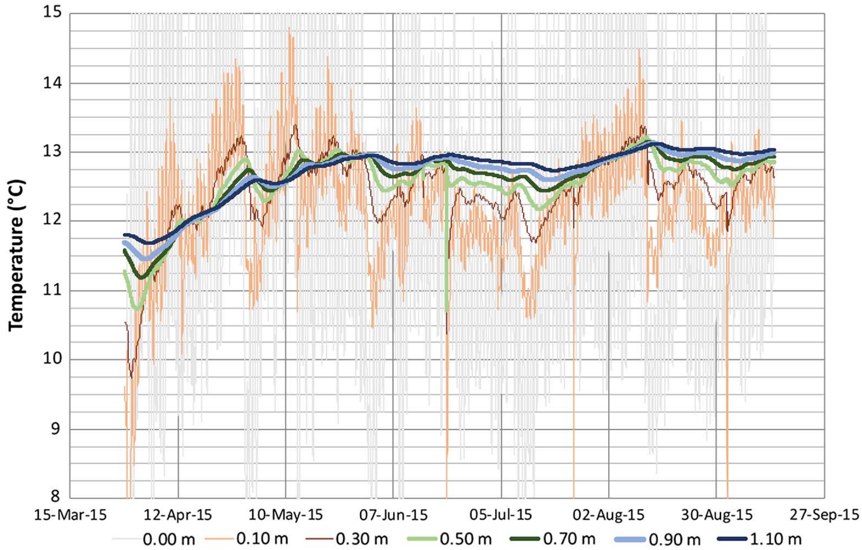

CARRAPATEENA

Figure 6 shows the Carrapateena temperature record in the frequency domain in the form of amplitude versus period (inverse of frequency) spectra for three of the six depths. The diurnal (one-day) signal stands out with an amplitude about one and a half orders of magnitude above the trend at all depths. 12-, 8-, and 6-h harmonics are also prominent at all depths; a 4.8-h harmonic is detected at 0.50 m and a 4-h harmonic at 0.10 m. All signals descend into "noise" at amplitudes between about 1×10^{-3} K and 3×10^{-2} K at the short period (high frequency) ends of the spectra. The lowest amplitudes correlate with the resolution of the digital sensors; about 2×10^{-4} K. As noted above, when normalized by a factor of $2/N$ (where N is the number of samples in the original time series), the amplitudes represent the "true" magnitude of each frequency's contribution to the original signal. Summing the normalized amplitudes of periods between 23.5 and 24.5 hr, for example, suggests a diurnal signal amplitude (half peak–trough) of 5.2 K at 0.10 m (**fig. 6*A***), which is consistent with the qualitative assessment of **figure 3** above. The normalized amplitudes suggest that the diurnal signal decayed to 0.11 K at 0.50 m (**fig. 6*B***) and 6×10^{-4} K at 1.10 m (**fig. 6*C***).

Figure 7 presents charts of $\ln(\frac{A_0}{A_z})$ and $\Delta\phi$ versus $\sqrt{z^2 \cdot \pi \cdot f}$ for frequency components with amplitudes (nonnormalized) greater than 0.1 K and for depth intervals of 0.10–0.50 m (**fig. 7*A***) and 0.10–1.10 m (**fig. 7*B***). Each chart includes the linear regression lines of best fit through the origin for both the amplitude and phase points and also notes their slopes and standard errors. **Figure 7*B*** shows a noticeable scatter in the points at the highest frequency (right-hand) end of the chart. Increasing the threshold amplitude to 0.5 K (**fig. 7*C***) reduced the scatter and improved the precision (lowered the standard error) of the calculated amplitude slope but decreased the precision of the phase slope.

Figure 8 presents charts of $\ln(\frac{A_0}{A_z})$ and $\Delta\phi$ versus $\sqrt{z^2 \cdot \pi \cdot f}$ for amplitudes greater than 0.1 K for intervals 0.10–0.30 m (**fig. 8*A***), 0.50–0.70 m (**fig. 8*B***), and 0.90–1.10 m (**fig. 8*C***). Each chart also shows the linear regression lines of best fit through the origin for both the amplitude and phase points and notes their slopes and standard errors. **Figure 8*D*** shows the chart for amplitudes > 0.5 K over the 0.90–1.10 m depth interval for comparison with **figure 7*C***.

The lowest frequency points lie on the x-axis to the right of the origin on all charts on **figures 7** and **8**. This is an artifact of the Hanning window (equation (4)), which effectively overprinted every record with a uniform low-frequency cosine wave before the FFT. We display the affected low frequency points on **figures 7** and **8** for

FIG. 6

Nonnormalized amplitude versus period spectra on log-log axes for Carrapateena at depths (*A*) 0.10 m, (*B*) 0.50 m, and (*C*) 1.10 m. Horizontal axis is period in days. Vertical axis is amplitude in kelvin. Each dot represents a single frequency component of the signal.

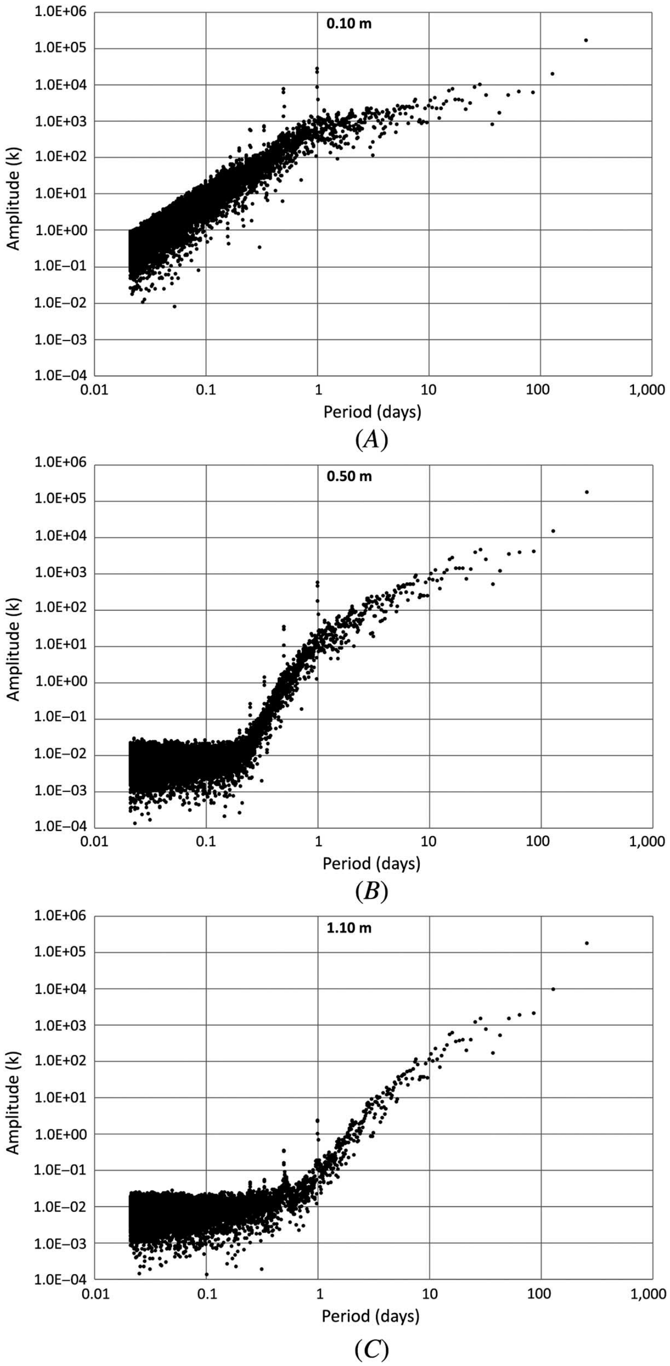

illustrative purposes and because they have minimal impact on the regression lines. The low-frequency points should, however, be excluded from subsequent slope calculations to maximize precision.

We note a constant offset between the phase and amplitude points on figure 8*C* and 8*D*. If not forced through the origin, the linear regression line of best fit through the amplitude points has a slope equivalent

FIG. 7

$\ln(\frac{A_0}{A_z})$ (green circles) and $\Delta\phi$ (blue triangles) versus $\sqrt{z^2 \cdot \pi \cdot f}$ charts for Carrapateena. (*A*) Depth interval 0.10–0.50 m for amplitudes greater than 0.1 K, (*B*) depth interval 0.10–1.10 m for amplitudes greater than 0.1 K, (*C*) depth interval 0.10–1.10 m for amplitudes greater than 0.5 K. Slopes and standard errors of lines of best fit through the origin are given on each chart.

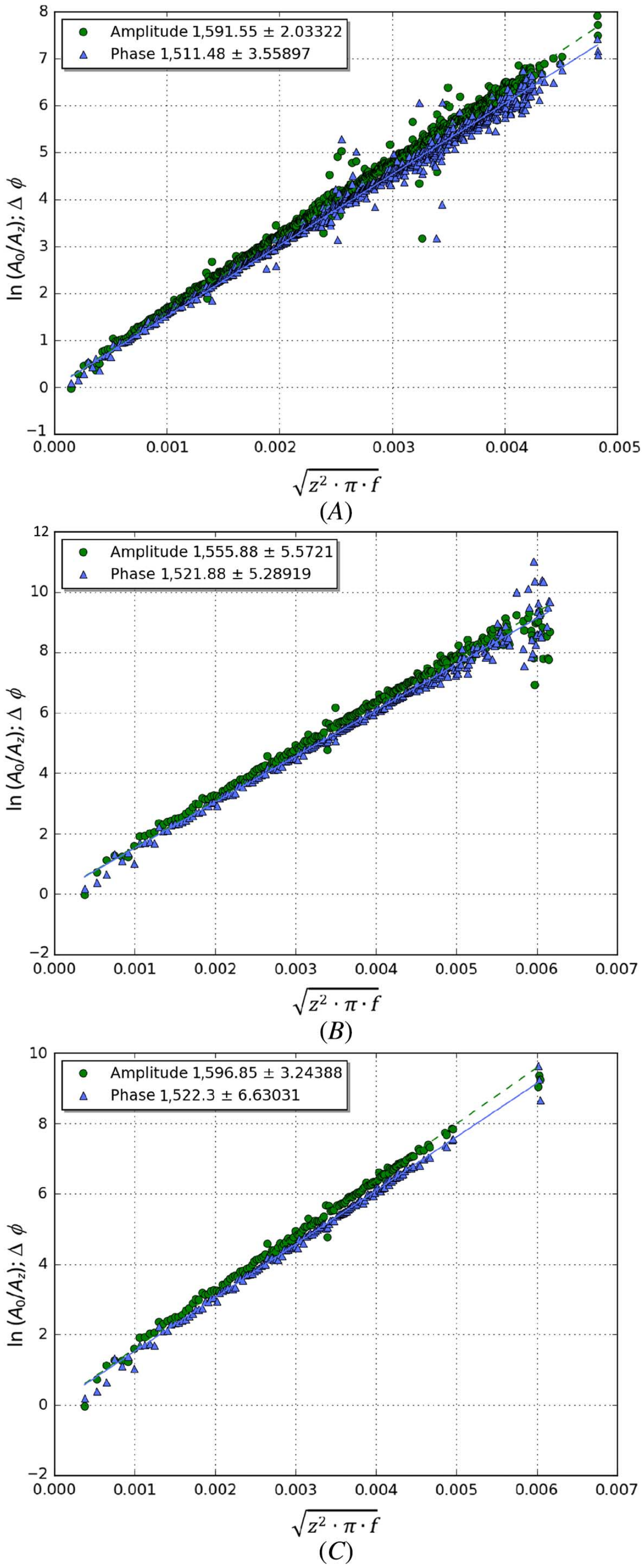

FIG. 8 $\ln(\frac{A_0}{A_z})$ (green circles) and $\Delta\phi$ (blue triangles) versus $\sqrt{z^2 \cdot \pi \cdot f}$ for Carrapateena. (*A*) Depth interval 0.10–0.30 m for amplitudes greater than 0.1 K, (*B*) depth interval 0.50–0.70 m for amplitudes greater than 0.1 K, (*C*) depth interval 0.90–1.10 m for amplitudes greater than 0.1 K, and (*D*) depth interval 0.90–1.10 m for amplitudes greater than 0.5 K. Slopes and standard errors of lines of best fit through the origin are given on each chart.

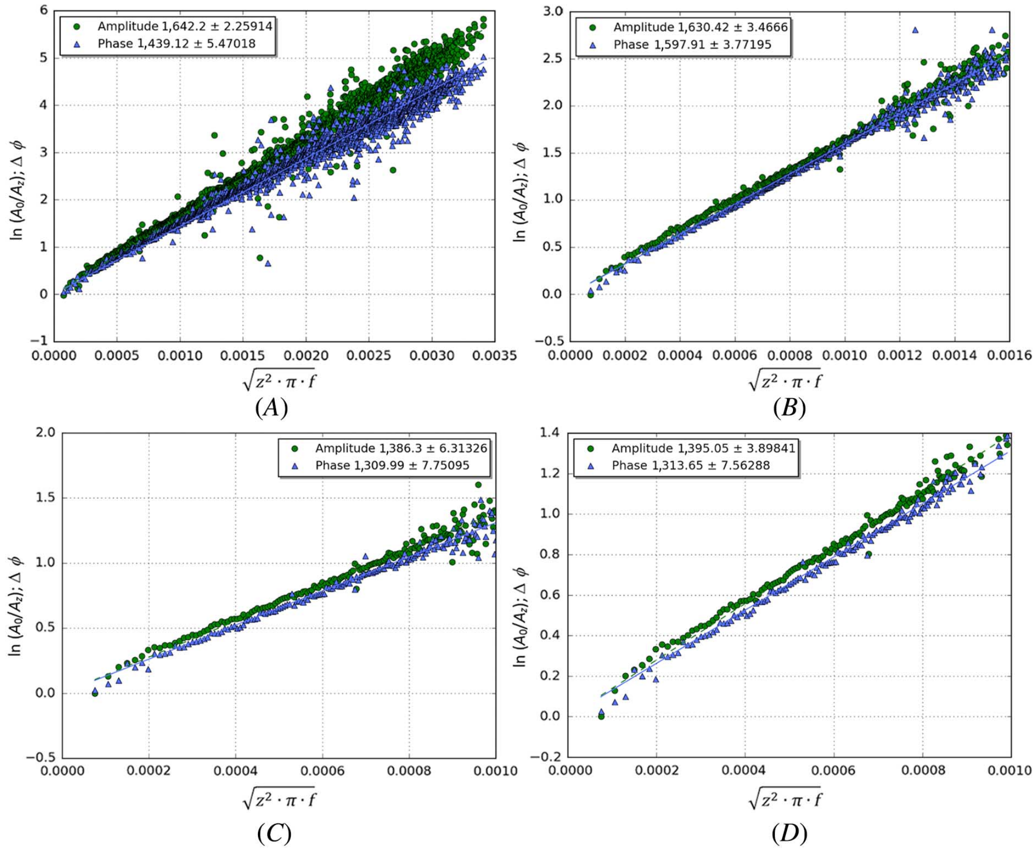

to that through the phase points, but crosses the *y*-axis at 0.0382. We have not investigated the cause of this in detail, so it remains unclear whether the offset is due to a physical mechanism or a numerical artifact.

According to equation (2), the slopes of the lines in figures 7 and 8 are equal to $\frac{1}{\sqrt{\kappa}}$. Table 1 lists the thermal diffusivity values and standard errors calculated for nine different depth intervals from both amplitude and phase data, and it also includes results for the slope both forced and not forced through the origin for the 0.9 –1.10 m interval. The standard errors are less than 1 % of the diffusivity values over most 0.20 m intervals, and a maximum of 1.5 % for the phase diffusivity of the 0.70–0.90 m interval. Table 1 also lists the averages of the two values for 0.20 m depth intervals between 0.30 and 1.10 m. The values are within ±3 % of their averages between 0.30 and 0.90 m, and within ± 6 % of their average for 0.90–1.10 m. The observed variance between phase and amplitude values might not reflect physical properties of the soil, but might instead be a computational artifact of forcing the regression lines through the origin. The phase and amplitude estimates of diffusivity for the 0.90–1.10 m interval converge to within ±2 % of their average if the slope of the amplitude points is *not* forced through the origin. In all cases, however, the precision is comparable to that reported by Popov et al. (2016) for laboratory measurements of thermal diffusivity.

Figure 9 shows the thermal diffusivity results as depth profiles with 95 % confidence intervals. Both phase and amplitude diffusivity were relatively consistent around 4×10^{-7} m^2/s between 0.30 and 0.90 m but

TABLE 1

Thermal diffusivity and uncertainty derived from amplitude, phase, and standard error at the Carrapateena site

Interval, m	Amplitude Diffusivity, m^2/s	Phase Diffusivity, m^2/s	Average Diffusivity[a], m^2/s
0.10–0.30	$3.708\ (\pm 0.010) \times 10^{-7}$	$4.828\ (\pm 0.037) \times 10^{-7}$	
0.10–0.50	$3.948\ (\pm 0.010) \times 10^{-7}$	$4.377\ (\pm 0.021) \times 10^{-7}$	
0.10–0.70	$3.827\ (\pm 0.009) \times 10^{-7}$	$4.176\ (\pm 0.020) \times 10^{-7}$	
0.10–0.90	$3.778\ (\pm 0.014) \times 10^{-7}$	$4.103\ (\pm 0.025) \times 10^{-7}$	
0.10–1.10[b]	$3.922\ (\pm 0.016) \times 10^{-7}$	$4.315\ (\pm 0.038) \times 10^{-7}$	
0.30–0.50	$4.199\ (\pm 0.009) \times 10^{-7}$	$4.245\ (\pm 0.010) \times 10^{-7}$	4.22×10^{-7}
0.50–0.70	$3.762\ (\pm 0.016) \times 10^{-7}$	$3.916\ (\pm 0.018) \times 10^{-7}$	3.84×10^{-7}
0.70–0.90	$3.837\ (\pm 0.043) \times 10^{-7}$	$4.044\ (\pm 0.062) \times 10^{-7}$	3.94×10^{-7}
0.90–1.10[b]	$5.138\ (\pm 0.029) \times 10^{-7}$	$5.795\ (\pm 0.067) \times 10^{-7}$	5.47×10^{-7}
0.90–1.10[b]	$5.946\ (\pm 0.098)^{c} \times 10^{-7}$	$5.795\ (\pm 0.067) \times 10^{-7}$	$5.87^{c} \times 10^{-7}$

Note: [a] For depth intervals with no clear evidence of nonconductive heat exchange; [b] These values calculated for amplitudes >0.5 K; [c] Amplitude value calculated from the slope of best fit line not forced through the origin.

FIG. 9 Amplitude (thin green) and phase (thick blue) diffusivity versus depth for the Carrapateena site, from Table 1. Dashed lines show 95 % confidence intervals. Red dashed lines over 0.90–1.10 m interval show amplitude diffusivity calculated from the best fit line not forced through the origin.

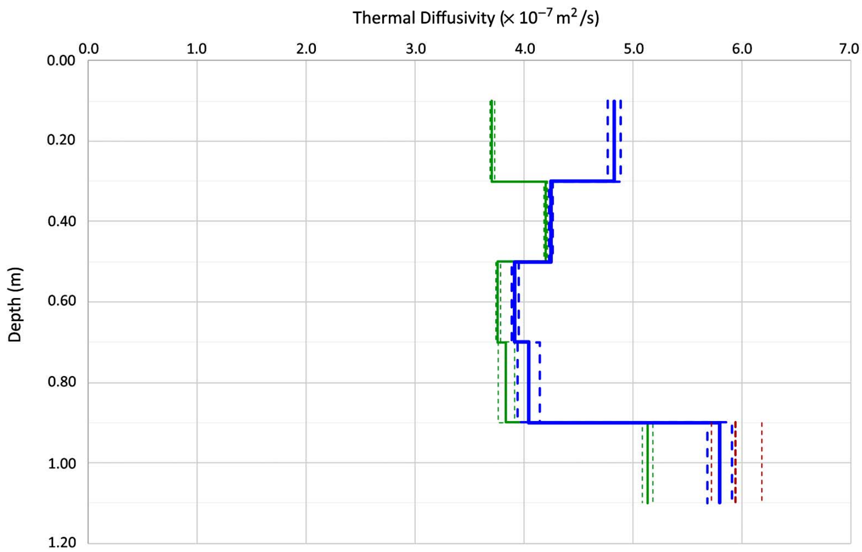

significantly higher between 0.90 and 1.10 m. As noted earlier, we did not collect a soil profile at the site, so the cause of the step change is speculative. However, it suggests a significant boundary between lithology or water content at about 0.90 m depth.

Diffusivity calculated from amplitude data is 23 ± 1 % lower than that calculated from phase data over the 0.10–0.30 m interval, and lower to lesser degrees over deeper intervals (for example, 1 ± 0.5 % lower from 0.30–0.50 m; 4 ± 1 % lower from 0.50–0.70 m; 5 ± 2.5 % lower from 0.70–0.90 m). In physical terms, that means the amplitude of the temperature signal decayed to a greater degree than would be expected from the observed phase lag. It could be explained by nonconductive heat exchange with the atmosphere during our measurements, consistent with the previous observations of Koo and Song (2008) and Rajeeva and Kodikara (2015), within 0.50 m of the ground surface. Mechanisms for nonconductive heat exchange include infrared radiation, bioturbation, transpiration, evaporation, condensation, air convection, and others. It is outside the scope of this article to interpret the relative contributions of each of these mechanisms, but they collectively enhance the exchange of heat between the soil and the atmosphere.

The relative contribution of nonconductive to conductive heat transport can be represented by the Peclet number (e.g., Beardsmore and Cull 2001). If we assume that nonconductive heat exchange affects the amplitude of each frequency component but not its phase, the Peclet number can be calculated from the difference between the amplitude and phase diffusivity estimates:

$$P_e = \frac{\kappa_p - \kappa_a}{\kappa_p} \tag{5}$$

where:

P_e = Peclet number, dimensionless,

κ_p = phase diffusivity, m^2/s, and

κ_a = amplitude diffusivity, m^2/s.

It is implicit in this assumption that the quantifiable component of nonconductive heat exchange is effectively instantaneous relative to the frequency band being interpreted. For example, the highest frequency component plotted on **figure 8*A*** for the 0.10–0.30 m interval at Carrapateena corresponds to a period of about 3 hr. Therefore, the nonconductive heat exchange assumed over this depth interval is the component that fully responded to soil temperature changes within approximately 1 hr. It follows that the quantifiable discrepancy between amplitude and phase responses is more likely to reflect the effects of radiation, evaporation, and condensation (rapid phenomena) rather than convection or transpiration (slower phenomena). The latter mechanisms would contribute to scatter on the plots.

In the case of the Carrapateena 0.10–0.30 m interval, $Pe = 0.232$. Including one standard error uncertainties, this implies that 23.2 ± 0.4 % (one standard deviation) of thermal energy was exchanged with the atmosphere from this depth interval by rapid nonconductive mechanisms.

PUEBLA

Figure 10 shows all seven amplitude (nonnormalized) spectra for the Puebla site. The 0.30 m, 0.50 m and 0.70 m spectra (**fig. 10*C*–*E***) are notably different to the others, and probable causes are discussed below. When normalized by a factor of $2/N$, the diurnal signal amplitude (half peak–trough) is 2.65 K at 0.00 m (**fig. 10*A***), decaying to 0.058 K at 0.30 m (**fig. 10*C***) and 8×10^{-5} K at 1.10 m (**fig. 10*G***).

Figure 11 shows two charts of $\ln(\frac{A_0}{A_z})$ and $\Delta\phi$ versus $\sqrt{z^2 \cdot \pi \cdot f}$ for each sensor interval. The left-hand charts show signals uniformly filtered for amplitudes greater than 0.8 K. The right-hand charts show signals filtered to amplitudes that minimize noise and standard errors, as listed in the figure caption.

The points on the Puebla charts (**fig. 11**) are more scattered than the Carrapateena charts (**fig. 8**). Several factors contribute to this. Firstly, the normalized magnitude of the Puebla signal at 0.10 m was about 30 % weaker than the Carrapateena signal across all frequencies. Secondly, the rate of amplitude attenuation with depth was higher at Puebla, meaning that the already-weak (relative to Carrapateena) surface signal became even weaker with depth. Thirdly, the record at Puebla was shorter than at Carrapateena, resulting in fewer frequency bins. Lastly, the Puebla temperature record was affected by at least four short-lived but prominent negative temperature spikes (evident in the 0.10 m record on **fig. 5**), which probably explain the unusual character of the amplitude spectra on **figure 10*C*–*E***. So, the Puebla data set was smaller (shorter record), lower quality (affected by temperature spikes), and contained less information (weaker amplitudes) than the Carrapateena data set. These differences resulted in higher uncertainties in the thermal diffusivity values.

Table 2 lists the thermal diffusivity values and standard errors calculated from the right-hand set of charts in **figure 11**. The standard errors of the diffusivities are between 4 and 13 % of their values over all depth intervals below 0.10 m. The averages are within 15 % of the individual estimates deeper than 0.10 m. The precision is significantly lower than the Carrapateena example, but acceptable for many applications.

FIG. 10 Nonnormalized amplitude versus period spectra on log-log axes for Puebla depths as labeled. Horizontal axis is period in days. Vertical axis is amplitude in kelvin. Each dot represents a single frequency component of the signal.

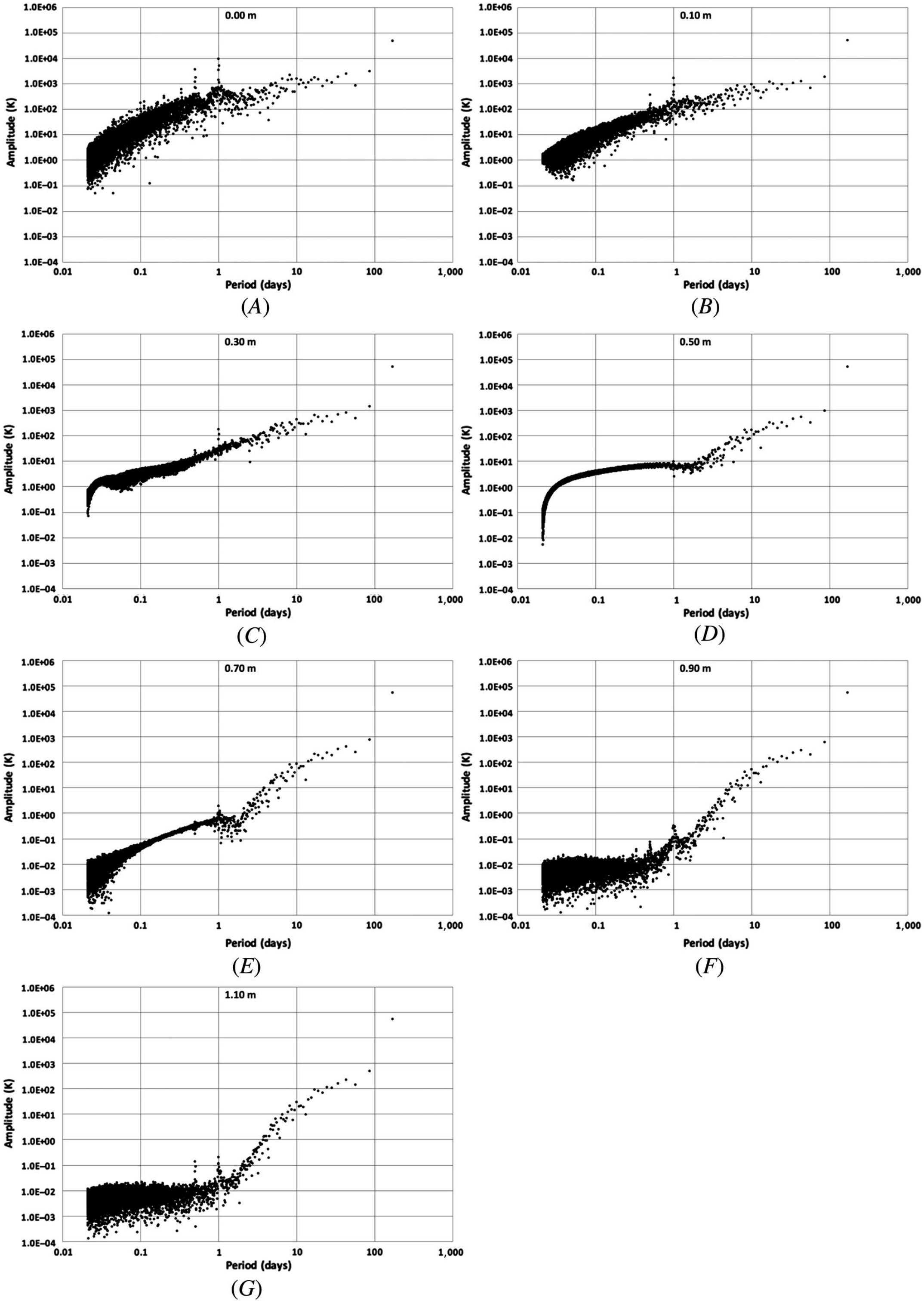

FIG. 11 $\ln(\frac{A_0}{A_z})$ (green circles) and $\Delta\phi$ (blue triangles) versus $\sqrt{z^2 \cdot \pi \cdot f}$ for Puebla depth intervals and amplitudes as follows: (*A*) 0.00–0.10 m, >0.8 K; (*B*) 0.00–0.10 m, >800 K; (*C*) 0.10–0.30 m, >0.8 K; (*D*) 0.10–0.30 m, >200 K; (*E*) 0.30–0.50 m, >0.8 K; (*F*) 0.30–0.50 m, >80 K; (*G*) 0.50–0.70 m, >0.8 K; (*H*) 0.50–0.70 m, >8 K; (*I*) 0.70–0.90 m, >0.8 K; (*J*) 0.70–0.90 m, >8 K; (*K*) 0.90–1.10 m, >0.8 K; (*L*) 0.90–1.10 m, >0.8 K. Slopes and standard errors of lines of best fit are noted on each chart.

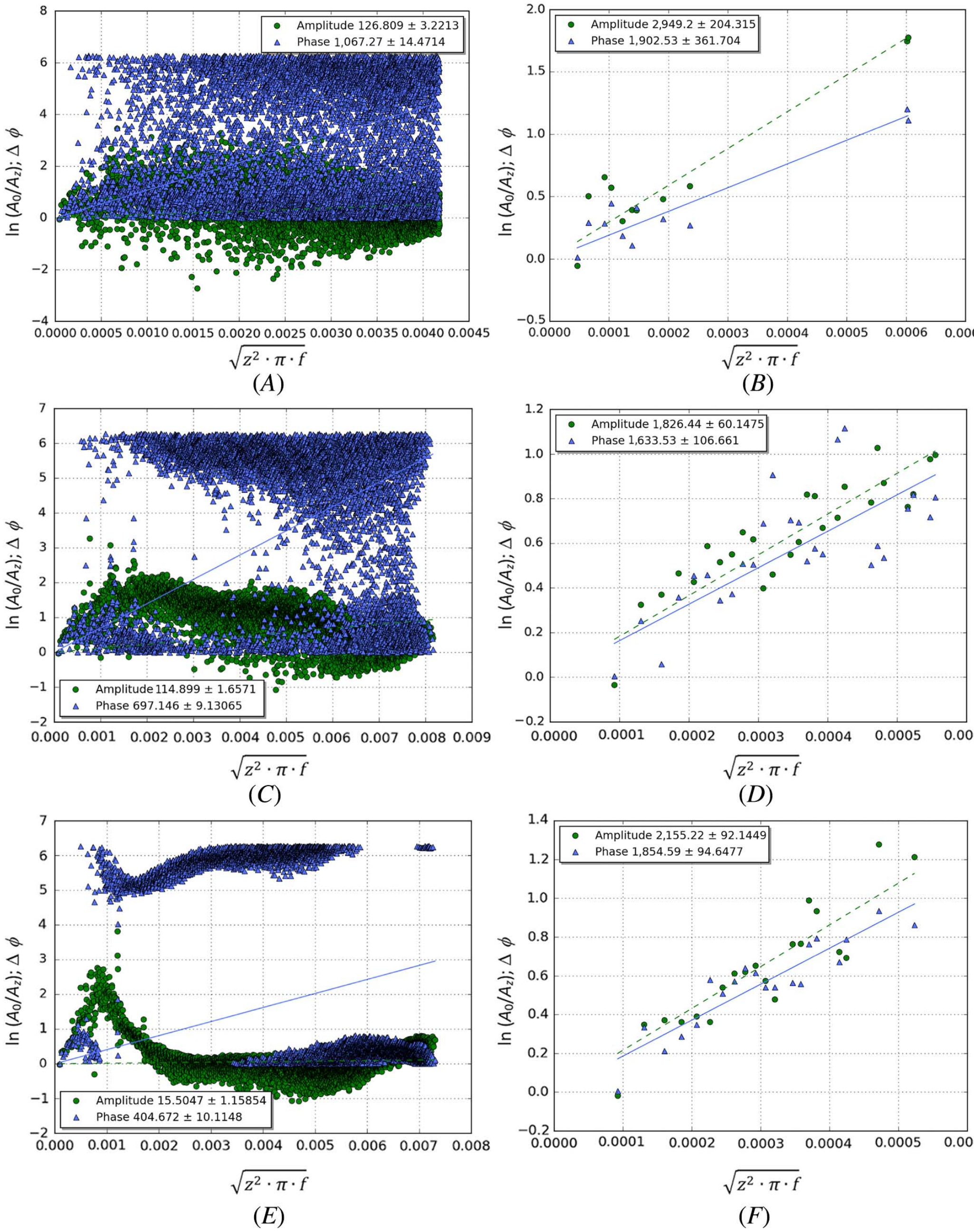

Figure 12 shows the amplitude and phase diffusivity depth profiles with 95 % confidence intervals. The confidence intervals of the two profiles overlap at all depths except 0.00–0.10 m. The thermal diffusivity between the surface and 0.70-m depth was significantly lower than at Carrapateena, consistent with the

FIG. 11 *Continued*

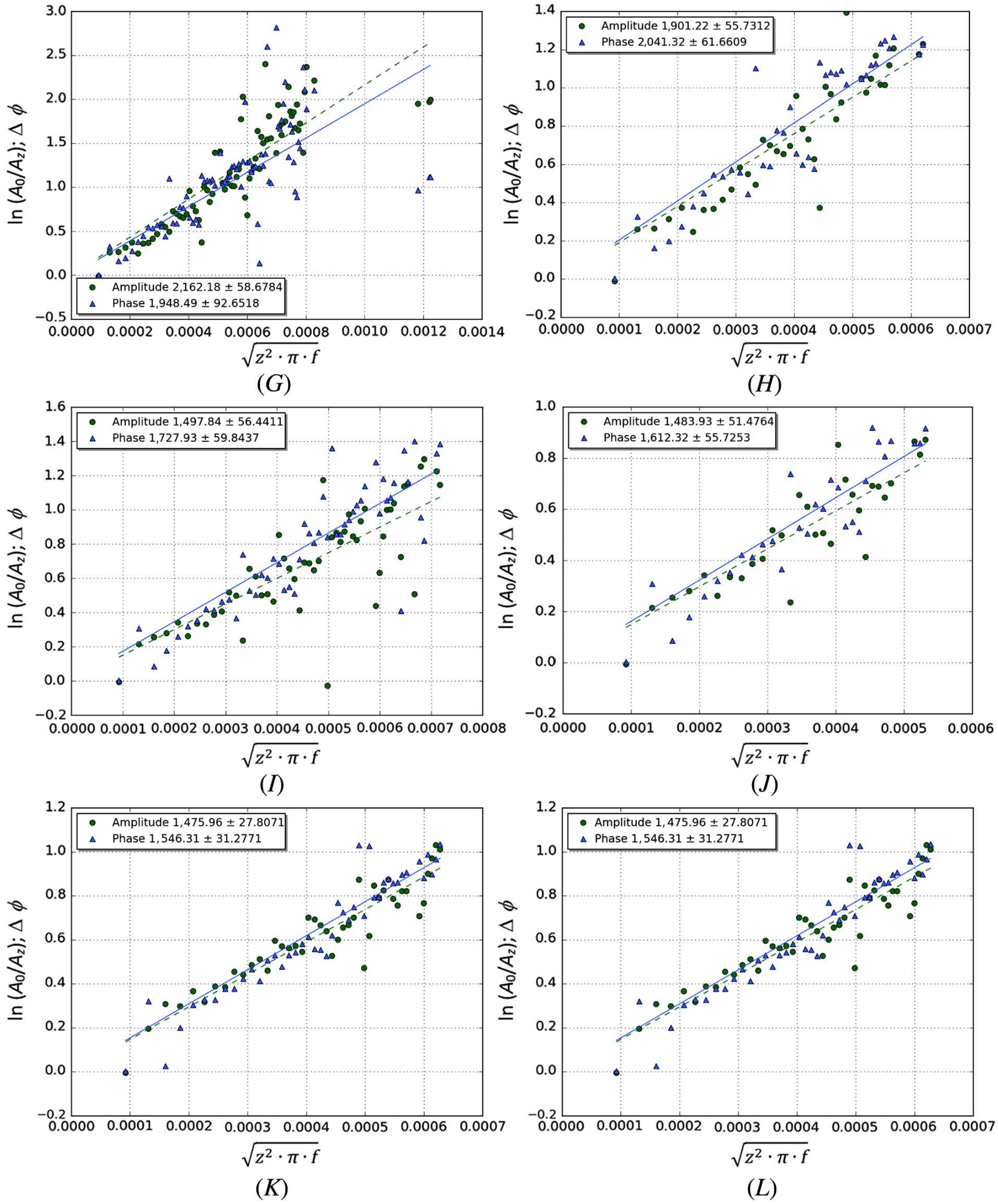

surface medium at Puebla—pine needle humus. Santoni et al. (2014) provided approximate thermal conductivity, density, and specific heat capacity values for the surface layer of forest beds beneath three different species of pine. **Table 3** presents thermal diffusivity of pine humus calculated from these values using equation (1). Low thermal diffusivity to a depth of 0.70 m at the Puebla site is consistent with compacted pine needle humus. The interface between the humus and underlying rocky soil probably lies at about 0.70 m.

TABLE 2
Thermal diffusivity and uncertainty derived from amplitude and phase data at the Puebla site

Interval, m	Amplitude Diffusivity, m^2/s	Phase Diffusivity, m^2/s	Average Diffusivity[a], m^2/s
0.00–0.10	$1.150\ (\pm 0.159) \times 10^{-7}$	$2.763\ (\pm 1.050) \times 10^{-7}$	
0.10–0.30	$2.998\ (\pm 0.197) \times 10^{-7}$	$3.748\ (\pm 0.489) \times 10^{-7}$	3.37×10^{-7}
0.30–0.50	$2.153\ (\pm 0.184) \times 10^{-7}$	$2.907\ (\pm 0.297) \times 10^{-7}$	2.53×10^{-7}
0.50–0.70	$2.767\ (\pm 0.162) \times 10^{-7}$	$2.400\ (\pm 0.145) \times 10^{-7}$	2.58×10^{-7}
0.70–0.90	$4.541\ (\pm 0.315) \times 10^{-7}$	$3.847\ (\pm 0.266) \times 10^{-7}$	4.19×10^{-7}
0.90–1.10	$4.590\ (\pm 0.173) \times 10^{-7}$	$4.182\ (\pm 0.169) \times 10^{-7}$	4.39×10^{-7}

Note: [a] For depth intervals with no clear evidence of nonconductive heat exchange.

FIG. 12 Amplitude (green) and phase (blue) diffusivity versus depth for the Puebla site, from Table 2. Dashed lines show 95 % confidence intervals.

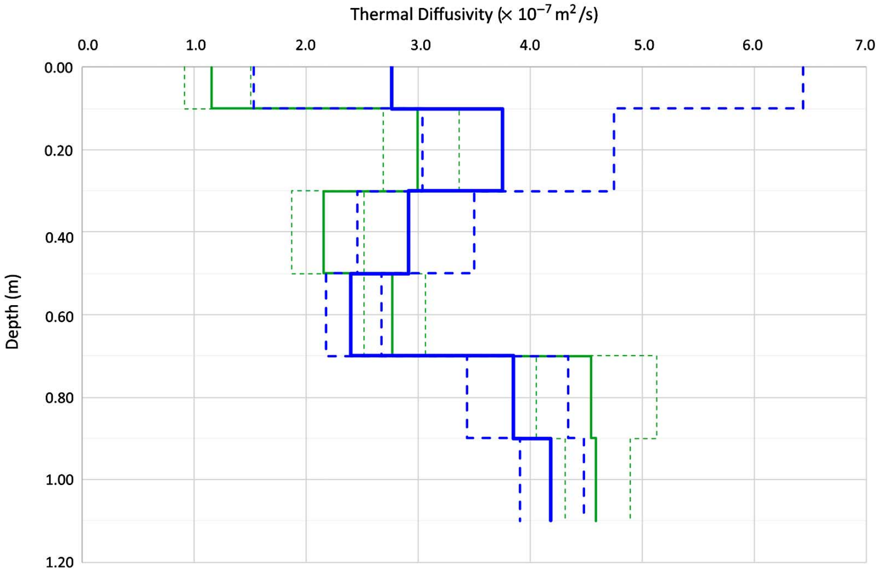

TABLE 3
Thermal properties of pine needles and thermal diffusivity calculated from equation (1)

Pine Species	Thermal Conductivity, W/(m K)	Specific Heat Capacity, J/(kg K)	Density kg/m^3	Thermal Diffusivity m^2/s
Pinus halepensis	0.1 ± 0.02[a]	$2{,}017 \pm 20$[b]	789 ± 19[c]	$0.63 \pm 0.15 \times 10^{-7}$
Pinus laricio	0.1 ± 0.02[a]	$1{,}827 \pm 18$[b]	485 ± 39[c]	$1.13 \pm 0.33 \times 10^{-7}$
Pinus pinaster	0.1 ± 0.02[a]	$1{,}868 \pm 19$[b]	511 ± 34[c]	$1.05 \pm 0.29 \times 10^{-7}$

Note: Data from Santoni et al. (2014); [a] Assumed 20 % uncertainty; [b] Assumed 1 % uncertainty; [c] Uncertainty stated by Santoni et al. (2014).

The Peclet number (equation (5)) calculated using the values and standard errors in Table 2 suggests that between 27 and 75 % of thermal energy was exchanged with the atmosphere from the top 0.10 m of the Puebla site through radiation, evaporation, and condensation, with a most likely figure of 68 %.

Thermal Diffusivity versus Time

The 260-d Carrapateena data set provided an opportunity to investigate the relationship between record length and the precision of thermal diffusivity calculations. Twenty-five samples were randomly selected from the full record for each of progressively greater sample lengths from 14 – 180 d. FFTs were performed on each sample, and diffusivities were calculated from the amplitude and phase components of the 0.10–0.30 m and 0.50–0.70 m depth intervals.

The standard errors (fig. 13) decreased with increasing sample length because longer samples captured a richer spectrum of frequencies to constrain the regression lines. The standard errors of the phase diffusivities were four times higher (a factor of four less precise) than the amplitude diffusivities over the 0.10–0.30 m interval (fig. 13*A* and 13*B*), but both recorded equal precision over the 0.50–0.70 m interval (fig. 13*C* and 13*D*). There was little improvement in precision at either depth beyond a sample length of 90 d.

Longer samples resulted in smaller variance in calculated thermal diffusivity (fig. 14). Over both depth intervals, the twenty-five 14-d samples gave a spread of values about $\pm 0.3 \times 10^{-7}$ m^2/s around the median amplitude diffusivity (fig. 14*A* and 14*C*) and $\pm 0.5 \times 10^{-7}$ m^2/s around the median phase diffusivity (fig. 14*B* and 14*D*). The results for 90-d samples were biased toward overestimating diffusivity relative to the median values, with the bias more pronounced for amplitude values. Amplitude diffusivity covered a range of about 0.3×10^{-7} m^2/s over the 0.10–0.30 m interval (fig. 14*A*) and 0.4×10^{-7} m^2/s over the 0.50–0.70 m interval (fig. 14*C*). Phase diffusivity covered ranges of about 0.6×10^{-7} m^2/s and 0.2×10^{-7} m^2/s over the 0.10–0.30 m (fig. 14*B*) and 0.50–0.70 m (fig. 14*D*) intervals, respectively.

FIG. 13 Standard errors of diffusivity calculated from 25 random samples of the Carrapateena record for each sample length from 14 – 180 d: (*A*) amplitude diffusivities, 0.10–0.30 m depth interval; (*B*) phase diffusivities, 0.10–0.30 m depth interval; (*C*) amplitude diffusivities, 0.50–0.70 m depth interval; and (*D*) phase diffusivities, 0.50–0.70 m depth interval. Solid lines are median values for each sample length.

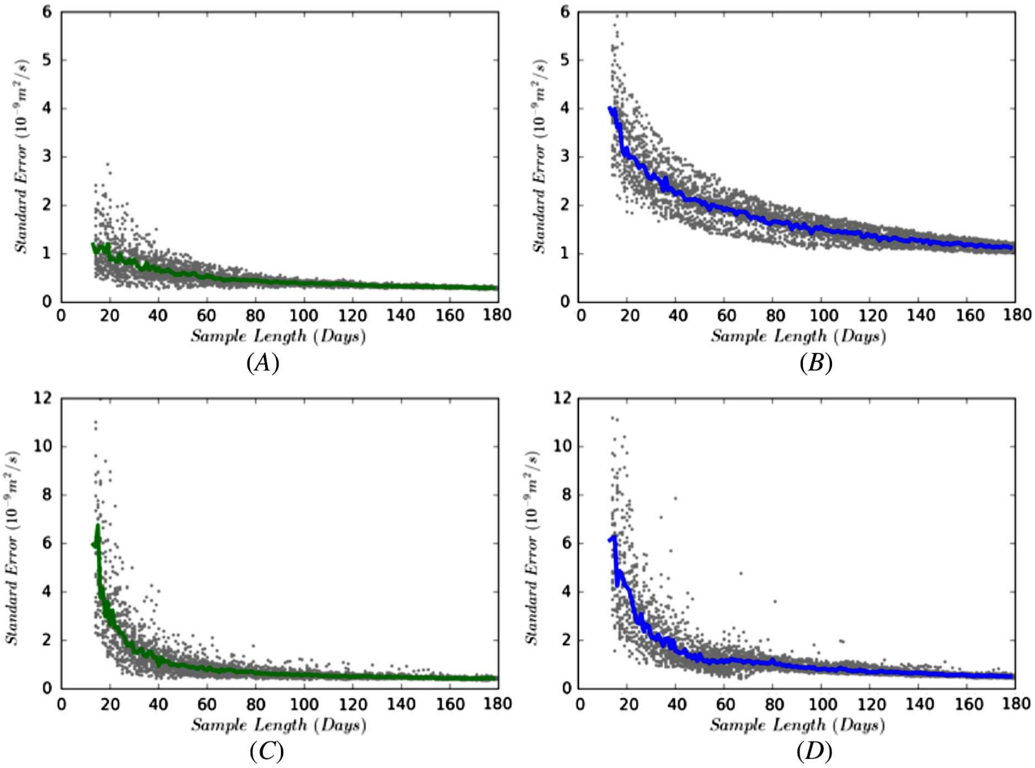

FIG. 14 Diffusivity calculated from 25 random samples of the Carrapateena record for each sample length from 14 – 180 d: (*A*) amplitude diffusivities, 0.10–0.30 m depth interval; (*B*) phase diffusivities, 0.10–0.30 m depth interval; (*C*) amplitude diffusivities, 0.50–0.70 m depth interval; and (*D*) phase diffusivities, 0.50–0.70 m depth interval. Solid lines are median values for each sample length.

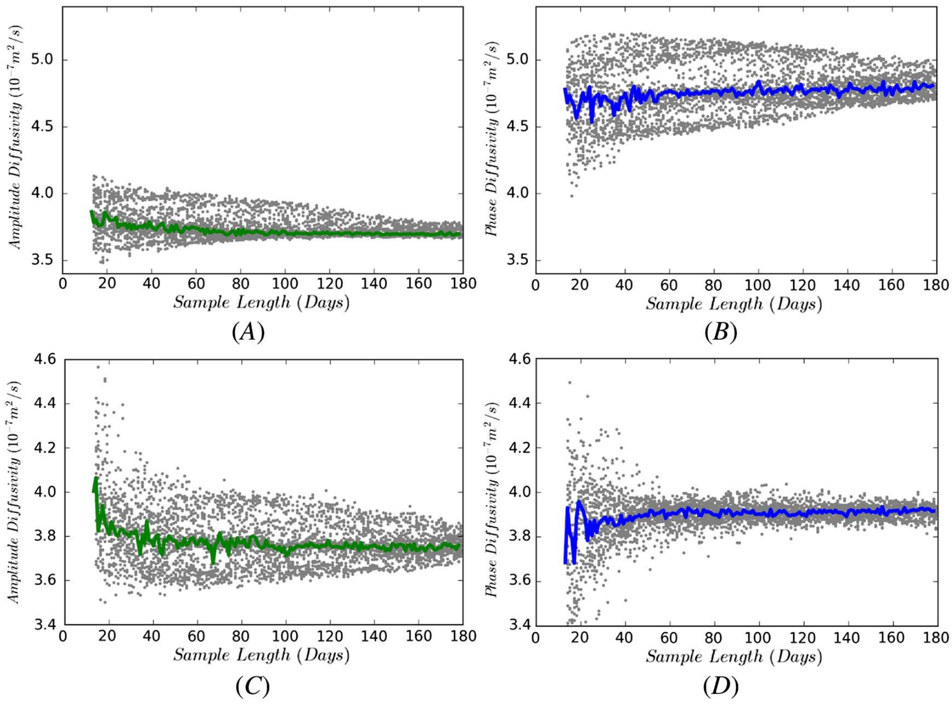

It is evident from **figures 13** and **14** that the variance in calculated diffusivities at different times greatly exceeded the standard errors of the measurements for all sample lengths. This suggests that at least part of the variance was due to variation in thermal diffusivity over time rather than measurement uncertainty. Furthermore, the plots in **figure 14** suggest that the phase and amplitude diffusivities varied between end-member values. For example, mean amplitude diffusivity between 0.10–0.30 m depth (**fig. 14*A***) over 21-d periods varied between about 3.5×10^{-7} m^2/s and 4.1×10^{-7} m^2/s, whereas phase diffusivity (**fig. 14*B***) varied between about 4.3×10^{-7} m^2/s and 5.2×10^{-7} m^2/s over the same depth and time intervals. These end-member values could represent the characteristic thermal diffusivity values for the soil under different physical conditions; for example, dry versus fully saturated soil, with diffusivities varying through time as soil moisture content varied between the two extremes.

To investigate this possibility, we calculated the amplitude and phase thermal diffusivities for a moving 3-week sample through time from the beginning to end of the Carrapateena record. **Figure 15** charts the results, with 95 % confidence intervals, for the 0.10–0.30 m (**fig. 15*A***) and 0.50–0.70 m (**fig. 15*B***) depth intervals.

Figure 15*A* indicates statistically significant changes in both amplitude and phase diffusivity through time. Although the variation through time of the two diffusivity estimates is not closely correlated, phase diffusivity remained consistently higher than the amplitude diffusivity over the record period. **Figure 15*B*** indicates uniform and equal amplitude and phase diffusivity (within 95 % confidence range) through time. It is beyond the scope of this article to analyze the results in detail, but the following observations are examples of the possible information content of the data.

FIG. 15 Amplitude (thin green) and phase (thick blue) diffusivity with shaded 95 % confidence intervals for 21-d samples finishing on the indicated date for the Carrapateena 0.10–0.30 m (top) and 0.50–0.70 m (bottom) depth intervals. Red dashed lines are the Peclet number (right axis) calculated from the mean diffusivities. Black spikes on the top chart show approximate daily rainfall (mm; right axis).

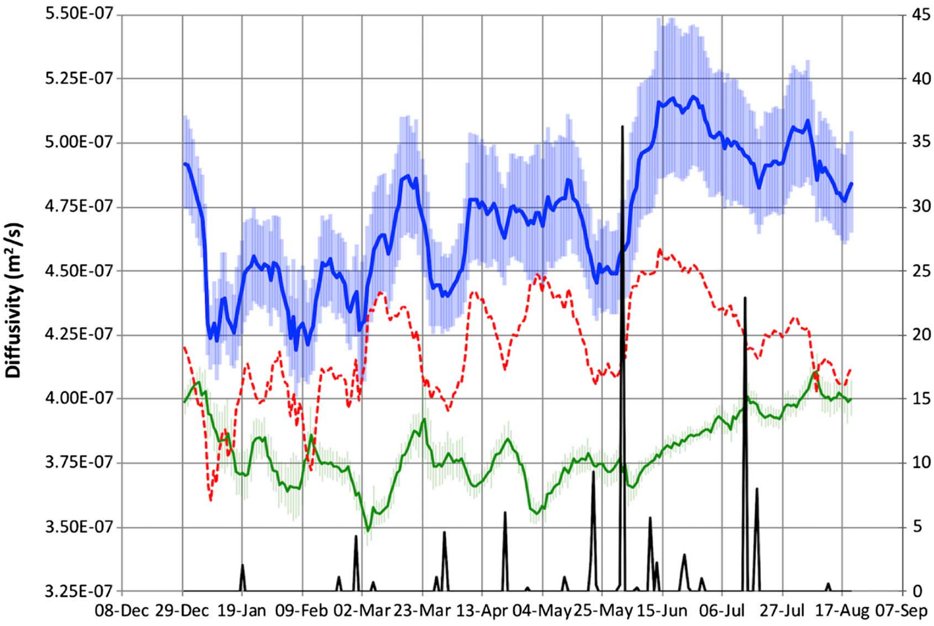

(*A*)

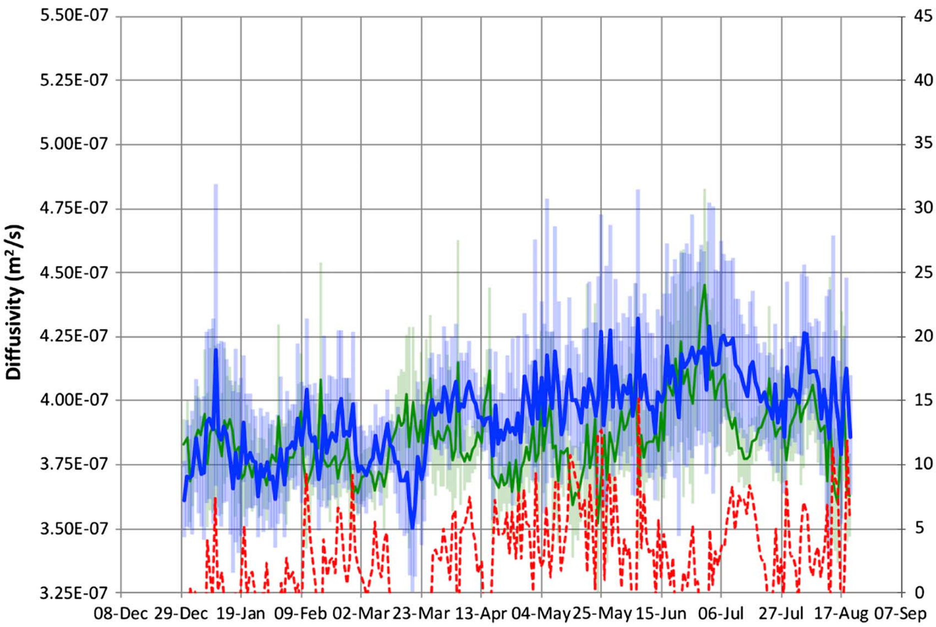

(*B*)

Figure 15*A* plots the average rainfall recorded across the Arcoona (31.02°S, 137.05°E), Pernatty (31.48°S, 137.48°E), and South Gap (31.63°S, 137.62°E) weather stations, 48 km WNW, 29 km S, and 47 km SSE, respectively, of the Carrapateena site (Bureau of Meteorology 2019a, 2019b, 2019c) as an approximation of local rainfall, for which no records exist. There is an apparent correlation between rainfall and increases in phase diffusivity in figure 15*A*, but no observed correlation in figure 15*B*. This is consistent with phase diffusivity being closely and positively correlated to soil moisture content, which was likely affected by rainfall more rapidly and strongly at shallower depths. The relationship between rainfall and amplitude diffusivity is more ambiguous, with some rainfall events associated in time with the onset of increases in amplitude diffusivity and others with the onset of decreases. This ambiguity could be due to overprinted effects of increased soil moisture and changes in evaporative and radiative processes.

The Peclet number mirrors the trend of phase diffusivity on figure 15*A* and suggests an increase in nonconductive heat exchange with the atmosphere after rainfall. This is consistent with increased evaporation from shallow depths after rainfall.

Concluding Remarks

The results indicate that ground temperature records collected over periods of weeks to months can constrain thermal diffusivity profiles through the top meter of ground to a precision comparable to laboratory measurements under controlled conditions. When interpreted in the frequency domain, a significant number of frequency bins with periods of days to weeks can be characterized in terms of amplitude and phase. The different frequency bins conform to the predictions of theoretical heat conduction equations to give consistent values of thermal diffusivity with confidence intervals of a few percentage points in both data sets we examined, representing different regolith types and climate zones. Furthermore, changes in thermal diffusivity over time can be monitored by interpreting moving, multiweek samples.

Values of thermal diffusivity quantified from amplitude information over the shallowest depth intervals were significantly lower than values quantified from phase information in the data sets we examined. The divergence can be attributed to nonconductive heat exchange with the atmosphere at the shallowest levels, and the proportion of heat exchanged with the atmosphere by radiation, evaporation, and condensation can be estimated at about 70 % from the top 0.10 m at Puebla and about 23 % from the 0.10–0.30 m interval at Carrapateena.

Our temperature data sets were high quality in terms of subhour sampling rate, millikelvin accuracy, and submillikelvin precision. Although not described in this article, we repeated our analyses using the same data sets rounded to the nearest centikelvin and decikelvin, and were able to reproduce the same values of thermal diffusivity within error range. Furthermore, the component frequencies that provided the most information in the data sets we examined corresponded to wavelengths of days to weeks, implying that sampling intervals of several hours could provide the same information as our subhourly sampling intervals. For these reasons, the method we describe should be broadly applicable to new or existing ground temperature data sets collected globally using off-the-shelf temperature sensors and data loggers.

The in situ soil thermal diffusivity values reported in this article were not independently validated. We developed our processing methodology long after the temperature data sets were collected. It was impractical to revisit the sites, but future work will seek to compare in situ measurements with laboratory measurements of recovered physical specimens.

Our results confirmed the observations of earlier researchers that phase and amplitude information from time-series ground temperature data may be inconsistent with a single value of thermal diffusivity, especially at shallow depths. The question of which thermal diffusivity estimate (phase or amplitude) is best could have different answers depending on the application. The magnitude of subsurface temperature variations in response to a periodic surface signal would be best modeled using the apparent thermal diffusivity inferred from amplitude data, which we interpret to incorporate the effects of rapid nonconductive heat exchange with the atmosphere. The timing of subsurface temperature events would be best modeled using the thermal diffusivity inferred from phase data. If both magnitude and timing are important, then the effective thermal diffusivities for both the amplitude and phase components of the temperature signal should be independently quantified and modeled.

Our methodology provides a new avenue to investigate the complex energy and mass exchanges between the atmosphere and soil. Our methodology could be applied to investigate relationships between thermal diffusivity (phase and amplitude components) and soil moisture as well as radiation and evaporation over time using suites of appropriate sensors alongside temperature sensors.

ONLINE DATA AND ACKNOWLEDGMENTS

The ground temperature data referred to and analyzed in this article are available from Beardsmore (2018a, 2018b). The University of Adelaide, Barrick Gold Australia, Oz Minerals, and the Government of South Australia assisted with the original collection of the Carrapateena data set. The Mexican Center for Geothermal Innovation assisted with collecting the Puebla data set. The manuscript benefitted greatly from thoughtful comments from two anonymous reviewers.

References

ASTM International. 2013. *Standard Test Method for Thermal Diffusivity by the Flash Method*. ASTM E1461–13. West Conshohocken, PA: ASTM International, approved September 1, 2013. https://doi.org/10.1520/E1461-13

ASTM International. 2016. *Standard Test Method for Calculating Thermal Diffusivity of Rock and Soil*. ASTM D4612–16. West Conshohocken, PA: ASTM International, approved May 1, 2016. https://doi.org/10.1520/D4612-16

ASTM International. 2017. *Standard Test Method for Thermal Conductivity and Thermal Diffusivity by Modulated Temperature Differential Scanning Calorimetry*. ASTM E1952–17. West Conshohocken, PA: ASTM International, approved September 1, 2017. https://doi.org/10.1520/E1952-17

Beardsmore, G. R. 2012. “Towards a Shallow Heat Flow Probe for Mapping Thermal Anomalies.” Paper presented at the 37th Workshop on Geothermal Reservoir Engineering, Stanford, CA, January 30-February 1, 2012.

Beardsmore, G. 2018a. “Carrapateena TLOG.csv (Version 1).” *University of Melbourne*. https://doi.org/10.26188/5b6bce14a6f31

Beardsmore, G. 2018b. “Puebla TLOG.csv (Version 1).” *University of Melbourne*. https://doi.org/10.26188/5b63e0ee98907

Beardsmore, G. R. and A. Antriasian. 2015. “Developing the ‘Heat Needle’: A Tool for Cost Effective Heat Flow Mapping.” Paper presented at the World Geothermal Congress, Melbourne, Australia, April 20–24, 2015.

Beardsmore, G. R. and J. P. Cull. 2001. *Crustal Heat Flow: A Guide to Measurement and Modelling*. Cambridge, UK: Cambridge University Press.

Beardsmore, G., L. Gutiérrez-Negrín, V. Garduño-Monroy, O. M. Espinoza-Ojeda, S. Almanza-Álvarez, A. Antriasian, and S. Egan. 2017. “Trial Deployment of a Surface Heat Flow Probe over the Los Azufres Geothermal Region, Mexico.” Paper presented at the 41st Workshop on Geothermal Reservoir Engineering, Stanford, CA, February 13–15, 2017.

Bording, T. S., S. B. Nielsen, and N. Balling. 2016. “The Transient Divided Bar Method for Laboratory Measurements of Thermal Properties.” *Geophysical Journal International* 207, no. 3 (December): 1446–1455. https://doi.org/10.1093/gji/ggw278

Bureau of Meteorology. 2019a. “Daily Rainfall Climate Data for Woomera (Arcoona), BoM Station Number 16000.” Climate Data Online, Product Code IDCJAC0009, Reference 39679028. Australian Government Bureau of Meteorology. http://web.archive.org/web/20190517010027/http://www.bom.gov.au/climate/data/

Bureau of Meteorology. 2019b. “Daily Rainfall Climate Data for Woomera (Pernatty Station), BoM Station Number 16036.” Climate Data Online, Product Code IDCJAC0009, Reference 39855188. Australian Government Bureau of Meteorology. http://web.archive.org/web/20190517010027/http://www.bom.gov.au/climate/data/

Bureau of Meteorology. 2019c. “Daily Rainfall Climate Data for Woomera (South Gap Station), BoM Station Number 16043.” Climate Data Online, Product Code IDCJAC0009, Reference 39855194. Australian Government Bureau of Meteorology. http://web.archive.org/web/20190517010027/http://www.bom.gov.au/climate/data/

Cheng, Q., Y. Sun, S. B. Jones, V. I. Vasilyev, V. V. Popov, G. Wang, and L. Zheng. 2014. “In Situ Measured and Simulated Seasonal Freeze–Thaw Cycle: A 2-Year Comparative Study between Layered and Homogeneous Field Soil Profiles.” *Journal of Hydrology* 519, part B (November): 1466–1473. https://doi.org/10.1016/j.jhydrol.2014.09.023

Craig, M. A. 2013. *Regolith Map of Australia*. Canberra: Geoscience Australia. http://web.archive.org/web/20190530054003/https://d28rz98at9flks.cloudfront.net/75626/REGOLITH_AUSTRALIA_edit1_400_Hires_WEB_Release.pdf

Harris, F. J. 1978. “On the Use of Windows for Harmonic Analysis with the Discrete Fourier Transform.” *Proceedings of the IEEE* 66, no. 1 (January): 51–83. https://doi.org/10.1109/PROC.1978.10837

Koo, M.-H. and Y. Song. 2008. “Estimating Apparent Thermal Diffusivity Using Temperature Time Series: A Comparison of Temperature Data Measured in KMA Boreholes and NGMN Wells.” *Geosciences Journal* 12, no. 3 (September): 255–264. https://doi.org/10.1007/s12303-008-0026-5

Middleton, M. F. 1993. “A Transient Method of Measuring the Thermal Properties of Rocks.” *Geophysics* 58, no. 3: 357–365. https://doi.org/10.1190/1.1443419

Popov, Y., G. Beardsmore, C. Clauser, and S. Roy. 2016. "ISRM Suggested Methods for Determining Thermal Properties of Rocks from Laboratory Tests at Atmospheric Pressure." *Rock Mechanics and Rock Engineering* 49, no. 10 (October): 4179–4207. https://doi.org/10.1007/s00603-016-1070-5

Rajeeva, P. and J. Kodikara. 2016. "Estimating Apparent Thermal Diffusivity of Soil Using Field Temperature Time Series." *Geomechanics and Geoengineering* 11, no. 1: 28–46. https://doi.org/10.1080/17486025.2015.1006266

Saavedra, M. and K. Takahashi. 2017. "Physical Controls on Frost Events in the Central Andes of Peru Using In Situ Observations and Energy Flux Models." *Agricultural and Forest Meteorology* 239 (May): 58–70. https://doi.org/10.1016/j.agrformet.2017.02.019

Santoni, P. A., P. Bartoli, A. Simeoni, and J. L. Torero. 2014. "Bulk and Particle Properties of Pine Needle Fuel Beds – Influence on Combustion." *International Journal of Wildland Fire* 23, no. 8: 1076–1086. https://doi.org/10.1071/WF13079

Singh, D. N. and M. V. B. B. G. Rao. 1998. "Laboratory Measurement of Soil Thermal Resistivity (Abs.)" *Geotechnical Engineering Bulletin* 7, no. 3: 179–189. http://web.archive.org/web/20190530061422/https://trid.trb.org/View/504294